A study of Co-Mn Phosphate supported with graphene foam as promising electrode materials for future electrochemical capacitors

*Abdulmajid A. Mirghni, Kabir O. Oyedotun, Badr A. Mahmoud, Oladepo Fasakin, Delvina J. Tarimo and Ncholu Manyala**

Department of Physics, Institute of Applied Materials, SARChI Chair in Carbon Technology and Materials, University of Pretoria, Pretoria 0028, South Africa.

*Corresponding author's email: ncholu.manyala@up.ac.za, Tel.: + (27)12 420 3549.

Abstract

Mn and Co are known for their redox storage mechanism depending on the kinetics of their ions, which is required to boost capacity values of the material electrodes for energy storage applications. However, to the best of our knowledge, Co-Mn phosphate material-based electrochemical capacitors have been rarely investigated. In this work, $CoMn(PO_4)_2$ synergized with graphene foam (GF) was synthesized following an easy, direct and low temperature hydrothermal method. The study investigated the synergy between Co, Mn and GF supported composite, with a strong P-O covalent tie occurring at the surface of the material, leading to a high degree of polarization and very low relaxation time. The $CoMn(PO_4)_2$/GF material tested as a half-cell could achieve a specific capacity of 58.15 mAh g^{-1} at 0.5 A g^{-1}. A $CoMn(PO_4)_2$/GF//AC hybrid device was made-up considering $CoMn(PO_4)_2$/GF and an activated carbon (AC) material as positive and negative electrodes, respectively. The $CoMn(PO_4)_2$/GF//AC hybrid device achieved a specific capacity of 45.89 mAh g^{-1}, specific energy of 51.53 Wh kg^{-1} and a corresponding specific power of 561.52 W kg^{-1} at 0.5 A g^{-1}. Furthermore, the device displayed a 95% capacity retention after 10000 GCD cycles at 12 A g^{-1} and showed an improved performance over its initial specific capacity after a voltage holding test for over 110 h at 2 A g^{-1}.

Keywords: Metal phosphate; electrochemical capacitor; Graphene; Co-phosphate, Mn-phosphate; storage devices.

1. Introduction

As a result of the tremendous shift towards green and sustainable sources for energy, for instance and limited to hydropower, wind and solar, countless efforts are being compensated to sustainable energy storage systems. These sustainable energy sources are friendly to the earth planet and with no side effects to human life. Unlike the conventional fossil fuel, they are safer, viable and more efficient energy supply systems. Electrochemical capacitors (ECs) are being acknowledged among the top promising devices for the future electrochemical storage system owing to their flexible charging-discharging dynamics, high specific power and longer cycling life compared to other electrochemical storage systems, for instance, fuel cells (FCs), and conventional rechargeable lithium-ion batteries (LiBs) [1,2,3,41].

Transition metal phosphates (TMPs) have Recently turn out to be a strong competitive and promising materials electrodes for ECs [4]. TMPs offer good charge storage capability, multiple valence states, open structure; cavities and channels, tend to own worthy charge storing capability and have, therefore, been examined as potential pseudocapacitive electrode materials [5,6,7]. The flexible geometry of phosphate structure groups can resist, avoiding the distortion resulting from any mechanical alteration by moving the locations of atoms and stabilizing the intermediary state of the transition metal's ions [8,9]. Both the single and bimetallic phosphates materials can be employed as electrodes for ECs application. P. K. Katkar synthesized a binder-free Mn-phosphate by means of single-pot adopting hydrothermal method, the material showed 145 F g^{-1} value of a specific capacitance of at 0.2 mA cm^{-1} tested in a neutral electrolyte of 1 M Na_2SO_4 [10].

Researchers have been indicated in some recently published work [11,12] that comparing bimetallic with single metallic phosphate electrode materials for the electrochemical capacitor, bimetallic phosphate materials are more capable and exhibiting superior performance. This could be due to the benefit of synergistic influence of joining two active metals as a bimetallic material. The two metals could be of highly faradic nature thereby, resulting in a very rich and effective redox reaction. For instance, in our previously published work [13], sodium-nickel phosphate was synthesized following a direct and easy co-precipitation method, the study brought out the synergy of Ni and Na cations together with conductive graphene foam. The material tested in 2

M $NaNO_3$ aqueous electrolyte could operate well in a wide potential window extended from 0.0 to 1.0 V vs Ag/AgCl and could receive a high value of 63.3 mA h g^{-1} specific capacity at 1 A g^{-1}. In other cases, the bimetallic phosphate could be a combination of one metal similar to EDLC in its electrochemical performance (pseudocapacitive) and another highly faradic metal, whereby, the electrochemical performance is expected to result in a synergy of the constituent metals, with a slightly different mechanism. For instance, in our previously published study [14], a promising material of nickel-cobalt phosphate produced via hydrothermal method used for supercapacitor has been reported. The study demonstrated the storage mechanism of Co-phosphate which possess similar features to EDLC and Ni-phosphate that mostly shows faradic features. Surprisingly, the synergy between Co-phosphate and Ni-phosphate based on their different storage mechanism revealed on the electrochemical outcomes of $NiCo(PO_4)_3$ where the material showed higher specific capacity than the individual Ni-phosphate and Co-phosphate with efficient pseudocapacitive behavior. The composite material exhibited a value of 86.4 mAh g^{-1} specific capacity at 1 A g^{-1} in 1 M KOH. Afterward, an assembly of hybrid device was done based on $NiCo(PO_4)_3$ composite and AC as positive and negative electrodes respectively, resulted in 34.8 Wh kg^{-1} specific energy, 377 W kg^{-1} specific power at 0.5 A g^{-1} correlated with high stability of 95% capacity retention after 10000 cycles at 8 A g^{-1}.

Herein, we report a hydrothermal synthesis of Co-Mn phosphate and its composite of graphene foam and their demonstration as potential electrodes for electrochemical capacitors applications. The adopted hydrothermal technique possesses a huge advantage for materials' morphological controls, with preferred physio-chemical properties thus resulting in enhanced electrochemical performances of the as-synthesized electrodes. It also offers significant merits like simplicity, cost effectiveness, high purity and crystallinity of synthesized materials, high reaction rate, and low operation temperature range in the presence of an appropriate solvent. The study explored the electrochemical properties of a combination of well-established pseudocapacitive metals (Co, Mn) in an aqueous medium (1 M KOH). Although, the discrete electrochemical storage mechanism of Mn and Co is by redox reaction however, each of the metals possesses semi-rectangular CV sweep due to the polarization initiated from polar nature of the materials [15]. The addition of 45 mg graphene foam (GF) to the synthesized cobalt-manganese phosphate produced a robust three-dimensional network ($CoMn(PO_4)_2$/GF), with an

anti-agglomeration property for long-time cycling. This improved short and quick ion/electron passage and sufficient electrode/electrolyte interaction. As result, the $CoMn(PO_4)_2$/GF composite showed a results in terms of current and discharge time, respectively, associated to the pure $CoMn(PO_4)_2$ which resulted in a specific capacity of 58.15 mAh g^{-1} at 0.5 A g^{-1}. An assembled hybrid supercapacitor device was built based on $CoMn(PO_4)_2$/GF and AC as positive and negative electrodes, respectively. The $CoMn(PO_4)_2$/GF//AC hybrid device achieved a specific capacity of 45.89 mAh g^{-1}, specific energy of 51.53 Wh kg^{-1} and a corresponding specific power of 561.52 W kg^{-1} at 0.5 A g^{-1}. Furthermore, the $CoMn(PO_4)_2$/GF//AC device was capable of retaining 95% capacity retention after being tested for continuously 10000 GCD cycles at 10 A g^{-1}. Likewise, the device exposed to a floating evaluation of over 110 h at 2 A g^{-1} and could show an improved performance over its initial specific capacity after a voltage holding test for over 110 h at 2 A g^{-1}. This outstanding stability of $CoMn(PO_4)_2$/GF//AC device is attributed to the synergy between $CoMn(PO_4)_2$ and GF and also due to stable chemical structure of $CoMn(PO_4)_2$ material, which contains strong P−O covalent bond. Besides, phosphate-based materials contain tetrahedral anion structural units $(PO_4)^{n-}$ associated with P−O bonds, generating oxygen octahedral sites occupied by other metal ions, which makes them structurally and chemically stable. In fact, P and O are readily form covalent bonds with other atoms and rarely exist in isolation. As a rule, each of these atoms form a characteristic number of covalent bonds with other atoms which hold the atoms together, therefore, stable molecules exist.

2 Experimental Section

2.1 Synthesis of $CoMn(PO_4)_2$ and $CoMn(PO_4)_2$/GF composites

The $CoMn(PO_4)_2$ was synthesized through a hydrothermal method. Initially, stoichiometric amount of $Co(NO_3)_2.6H_2O$, $Mn(CH_3CO).4H_2O$ and $(NH_4)PO_4$ were dissolved in 20 ml deionized water (DW) separately. The $Co(NO_3)_2.6H_2O$ and $Mn(CH_3CO).4H_2O$ solutions were mixed and subjected to stirring for 30 min. The $(NH_4)PO_4$ solution, which is the source of PO_4 was added dropwise into the mixture while stirring at room temperature. The mixed solution was then transferred into a Teflon-lined stainless-steel autoclave and placed in an electric oven at 180 ^oC for 6 h. The recovered sample was filtered, washed with DW and dried in an atmospheric oven at 60 ^oC for 12 h. The recovered powder sample was referred to as $CoMn(PO_4)_2$. Scheme 1 shows

the steps for the synthesis of $CoMn(PO_4)_2$. Thereafter, the $CoMn(PO_4)_2$/GF composite material was further synthesized with addition of an optimized mass (45 mg) of GF to form a composite material designated as $CoMn(PO_4)_2$/GF following the same procedure as already stated in earlier study [16]. In brief, different masses (15 mg, 30 mg, 45 mg and 60, respectively) of the as-prepared GF were dispersed in 100 mL of deionized water by ultra-sonication for 18 h at room temperature. Thereafter, the procedure for the preparation of $CoMn(PO_4)_2$ material was followed by adding a stoichiometric amount of $Co(NO_3)_2.6H_2O$, $Mn(CH_3CO).4H_2O$ and $(NH_4)PO_4$ and then stirred for 30 min for homogeneity. The resulting homogeneous mixture was transferred into a Teflon-lined stainless-steel autoclave for hydrothermal process at 180 °C for 6 h. The recovered solid sample designated as $CoMn(PO_4)_2$/GF was washed with deionized water and dried overnight at 60 °C. The added GF was to enrich the electrical conductivity of $CoMn(PO_4)_2$ in this work and was synthesized via chemical vapour deposition (CVD) system already discussed in our previously published work [16].

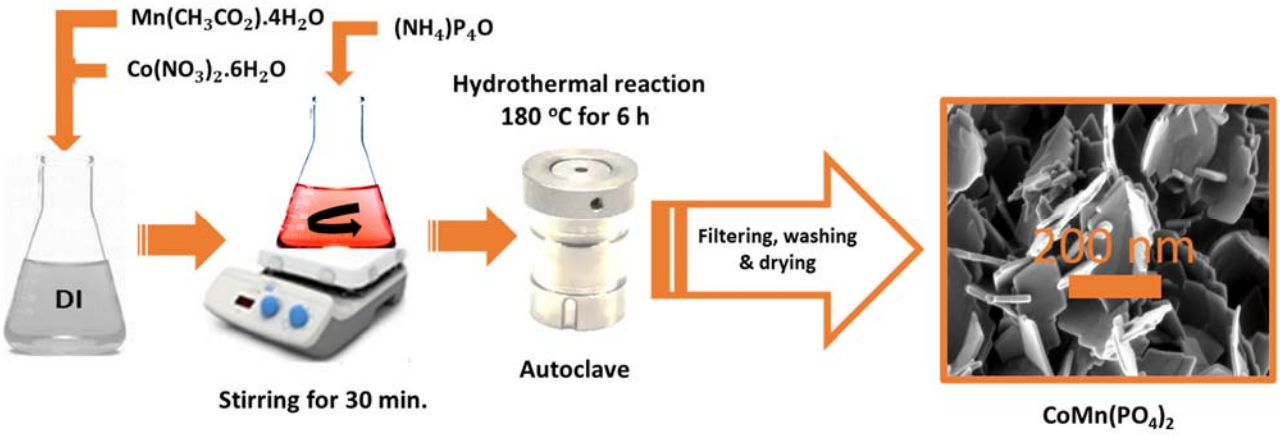

Scheme 1: Preparation steps of $CoMn(PO_4)_2$ material

2.2 Synthesis of activated carbon (AC)

Waste cocoa pods was collected from a dumping site in a farmland and used as source for carbon material. The cocoa pods collected was washed repeatedly with distilled water and acetone to avoid any possible dirt that can naturally be attached to the sample, thereafter, the sample dried at 60 °C for 24 h. After removing dirt, the sample crushed smoothly. A 10 g of the sample was

soaked in in 100 ml of DW having 10 ml of 0.5 M sulphuric acid for dehydration and to remove contaminants. The mixture was sealed in 120 ml autoclave, stainless steel and heated up to 160 ^{o}C for 12 h. The recovered material was removed from the oven and left to cool naturally to room temperature, and then washed several times with DI water followed by drying at 80 ^{o}C for 48 h. A pallet potassium hydroxide (KOH) was added to the product in a mass ratio of 1:1 and mixed in a gate mortar. The sample was then activated at 700 ^{o}C at a ramping rate of 5 ^{o}C/min for a period of 60 min in a flow of argon gas. The recovered carbonized material was soaked in 3 M hydrochloric acid overnight to neutralize remaining KOH. Then the sample was filtered and washed with deionized water regularly to reach a pH of 7. The final product was obtained after the sample has been dried completely using an oven for 24 h at 60 ^{o}C.

2.3 Characterizations and electrochemical analysis

The structural and crystalline nature of the samples were all examined via X-ray diffraction (XRD) (Bruker BV with 2D Phaser Benchtop, reflection geometry), 2ϑ = 10–65°, requisition time: 5.240 s per step, radiation source: Fe filtered Co Kα1 (λ = 0.1789 nm), operates at 30 mA and 50 kV. For molecular bonding analysis, A Confocal Raman Microscope with following descriptions was used, Model: WITec alpha 300 R Germany, Laser wavelength: 532 nm, laser power: 4 mW, spectral acquisition: 120 s. An X-ray photoelectron spectroscopy (XPS) analyzer (Versa Probe 5000 spectrometer initiated with a 100 µm monochromatic Al-Kα exciting source) was employed to measure the electronic states of the surface elements present within the composite sample. To attain the morphology of the samples, field emission scanning electron microscope (FE-SEM) was used with Model: A Zeiss Ultra plus 55 Germany, Carl Zeiss, Oberkochen, operates at 2.0 kV accelerating voltage. The specific surface area (SSA) and pore size distribution (PSD) analysis of the samples were performed by using a Discrete Fourier transform (DFT) model via the aid of a Quantachrome (NOVAtouch NT 2LX-1, Volts 220, USA) operated with the Quantachrome TouchWin Software Version: 1.22. The TEM analysis was obtained by JEOL JEM-2100F transmission electron microscopy operated at 200 kV. The samples were dispersed in ethanol under sonication for 30 minutes, therefore, the homogeneous solution was dropped uniformly on copper grids for examination. The electrode materials for 3-electrode measurement were prepared as follow: a combination of 80%, 10% and 10% of active (prepared) material,

polyvinylidene difluoride (PVDF) and carbon black respectively was mixed to form a slurry in the presence of some drops of 1-methyl-2- pyrrolidinone (NMP) as a solvent. The PVDF serves as a binder while carbon black was added to compensate for the reduction of conductivity resulted from an addition of PVDF. The slurry was pasted on 1 cm^2 nickel foam current collector. The pasted current collector was dried for 12 h at 60 ^oC in an electric oven to dry off the NMP. The final active mass-loaded to the electrode was weighted to be 3 mg cm^2. The 3-electrode system was explored to examine the as-prepared material in aqueous 1 M KOH as electrolyte, Ag/AgCl (3 M KCl saturated) as reference electrode, the active material working electrode under investigation, and glassy carbon as a counter electrode. To understand the storage mechanism of the materials, cyclic voltammetry (CV), galvanostatic charge-discharge (GCD) and electrochemical impedance spectroscopy (EIS) were measured. The EIS was measured in a frequency range between 100 KHz and 1.01 Hz and potential amplitude of zero. All the electrochemical measurements were carried out employing VMP-300 potentiostat, Knoxville, US Bio-logic instrument, associated with EC-lab software.

The specific capacity Q_s (mAh g^{-1}) and specific capacitance C_s (F g^{-1}) were calculated from the GCD curve using the following equation (1) and (2) respectively:

$$Q_S = \frac{q}{3.6 \times m} \quad \text{..... (1)}$$

$$C_s = \frac{q}{m \times \Delta V} \quad \text{..... (2)}$$

Where q is the charge, m is active mass and ΔV is the operating potential.

The charge storage mechanisms of $CoMn(PO_4)_2$ and AC are different, therefore, charge balance is required. Equations (3) and (4) below are applied to assure that the quantities of charges in the positive and negative electrodes are equal:

$$q_+ = q_- \quad \text{..... (3)}$$

Based on Eq. (1) and (2), the positive (q_+) and negative (q_-) charges can be expressed as function of specific capacity and specific capacitance respectively [17]:

$$3.6 \times m_{+} \times Q_s = m_{-} \times \Delta V_{-} \times C_s \Rightarrow \frac{m_{+}}{m_{-}} = \frac{\Delta V_{-} C_{S-}}{3.6 \times Q_s} \quad \text{..... (4)}$$

Where m_+ and m_- are the active masses loaded for the positive and negative electrodes respectively. Eq. (4) was applied to estimate the mass-ratio of both electrodes, therefore, $m_+:m_-$ was obtained to be 1:1.4. Based on this ratio, the masses of $CoMn(PO_4)_2$ and AC are 2.1 and 2.9 mg cm^{-2}, respectively, with device's total mass as 5.0 mg cm^{-2}. The $CoMn(PO_4)_2$/GF//AC hybrid device was assembled by using a standard 2025 grade coin cell with a Watman Celgard paper-based separator and 1 M KOH used as electrolyte, with the $CoMn(PO_4)_2$/GF and AC electrode acting as positive and negative electrodes, respectively. The assembled cell was impacted with a metallic spacer and spring to ensure tight contact in CR2025 grade coin cell.

Specific energy E_d *(Wh* kg^{-1}*)* and specific power P_d *(W* kg^{-1}*)* are two significant factors for assessing device's performances therefore, the following formulae (5) and (6) were applied to estimate the values of E_d *and* P_d:

$$E_d = \frac{i}{3.6m} \int V dt \quad \text{..... (5)}$$

$$P_d = 3600 \frac{E_d}{\Delta t} \quad \text{..... (6)}$$

Where $I = \frac{i}{m}$ denotes specific current and consequently, *I(mA)* is the current applied to the device while *m(mg* cm^{-2}*)* denotes the mass of the electrodes, *Δt(s)* denotes discharge time and $\int V dt$ denotes device's area under the discharge curve.

3 Results and discussion

Figure 1(a) represents XRD pattern of $CoMn(PO_4)_2$ measured in the range 2θ = 10° to 2θ = 65° plotted with the standard phase crystal. The mineralogy was determined by selecting the best–fitting pattern from the ideal matching Inorganic Crystal Structure Database (ICSD) database to the measured diffraction pattern, using Visualization Molecular Structure Diamond Crystal (VMSD) software. The peaks of the pattern are in coherence with the standard, according to the

ICSD card number: 00-052-1090, having the following specifications: chemical formula $Co_{1.25}Mn_{1.75}(PO_4)_2$ indicating a Co to Mn atomic ratio of ~ 1 : 1, space group: P, crystal system: Orthorhombic, cell parameters a = 9.4810 (Å), b = 9.9160 (Å), c = 8.6800 (Å), α = 90.0000°, β = 90.0000°, γ = 90.0000°. This is also supported by wt% from EDX analysis shown in the inset to figure 3 (I). Quantification of the sample could not be performed as phase $Mn_{1.75}Co_{1.25}(PO_4)_2$ is an old entry and does not contain structure data. The noticed peaks appeared sharp and narrow, indicating the high level of crystallinity of the material[18, 19]. The XRD spectrum measured in an angular range of 10° to 65° illustrates the appearance of peaks at angular positions 2θ equals ~ 12.73, 14.95, 22.12, 25.69, 26.86, 31.44, 35.38, 41.11, 47.94, 51.07, 52.85, 58.63, and 63.21° corresponding to the reflection planes 010, 110, 200, 012, 211, 030, 131, 321, 240, 402, 332, 250 and 105, respectively, indexed in line with an ICSD card number: 00-052-1090 for $CoMn(PO_4)_2$. Figure 1(b) represents XRD patterns of $CoMn(PO_4)_2$ plotted together with $CoMn(PO_4)_2$/GF composite. The figure confirms that both $CoMn(PO_4)_2$ and $CoMn(PO_4)_2$/GF share similar XRD patterns. However, the $CoMn(PO_4)_2$/GF composite material portrays an extra peak at 2θ = ~ 26.3°, which is attributed to a carbon and proved the existence of graphene foam in the $CoMn(PO_4)_2$/GF composite [20]. The Raman spectra of $CoMn(PO_4)_2$ and $CoMn(PO_4)_2$/GF are shown in Fig. 1(c). A formation of CoO and MnO_2 are observed in the $CoMn(PO_4)_2$ spectrum. The peak at ~ 483.45 cm^{-1} is owed to the stretching mode of Co-O, while the peaks at ~ 516.55 cm^{-1} and ~ 533.77 cm^{-1} are ascribed to the twisting modes of O-Mn-O [21,22]. The powerful peak wit high intensity at ~ 952.86 cm^{-1} is well-known and consigned to the symmetric stretching vibration mode of P-O-P [23]. All the modes approve the successful production of $CoMn(PO_4)_2$ material. An extra G and 2D peaks at 1520 and 2449 cm^{-1}, respectively, were seen in the $CoMn(PO_4)_2$/GF composite sample. These peaks are assigned to C-C vibrational mode and double resonance peak of carbon respectively [24]. The N_2 adsorption-desorption analysis was reported to estimate the specific surface area and pore size distribution (PSD) of the samples. Fig. 1(d) displays the isotherm and PSD of $CoMn(PO_4)_2$ and $CoMn(PO_4)_2$/GF samples. From the isotherm, $CoMn(PO_4)_2$ and $CoMn(PO_4)_2$/GF samples exhibit a type III behavior with an H3-type hysteresis loop which appeared to be convex to the X-axis demonstrating both samples having mesopores dominantly [25]. Figure 1(e) represents the pore size distribution curve of CoMn(PO4)2 and CoMn(PO4)2/GF was obtained using DFT method in the range of 0-9 nm. The PSDs of both materials revealing the

presence of mesopores, in line with the isotherms of the samples. The specific surface area values of $CoMn(PO_4)_2$ and $CoMn(PO_4)_2$/GF were estimated to be 8.2 $m^2 g^{-1}$ and 16.1 $m^2 g^{-1}$ respectively. The improved specific surface area recorded for $CoMn(PO_4)_2$/GF is owed to the attendance of GF within the composite sample. The integration of GF into $CoMn(PO_4)_2$ structure has resulted in a synergistic effect, enabling a defined nanosheet that emanated via the addition of GF, therefore, enhances the flow of electrolyte ions in and out of the material. This, in turn reduces the possibility of particle aggregation and minimizes ion diffusion resistance. Accordingly, the electrochemical response of $CoMn(PO_4)_2$/GF composite material is likely to be enhanced.

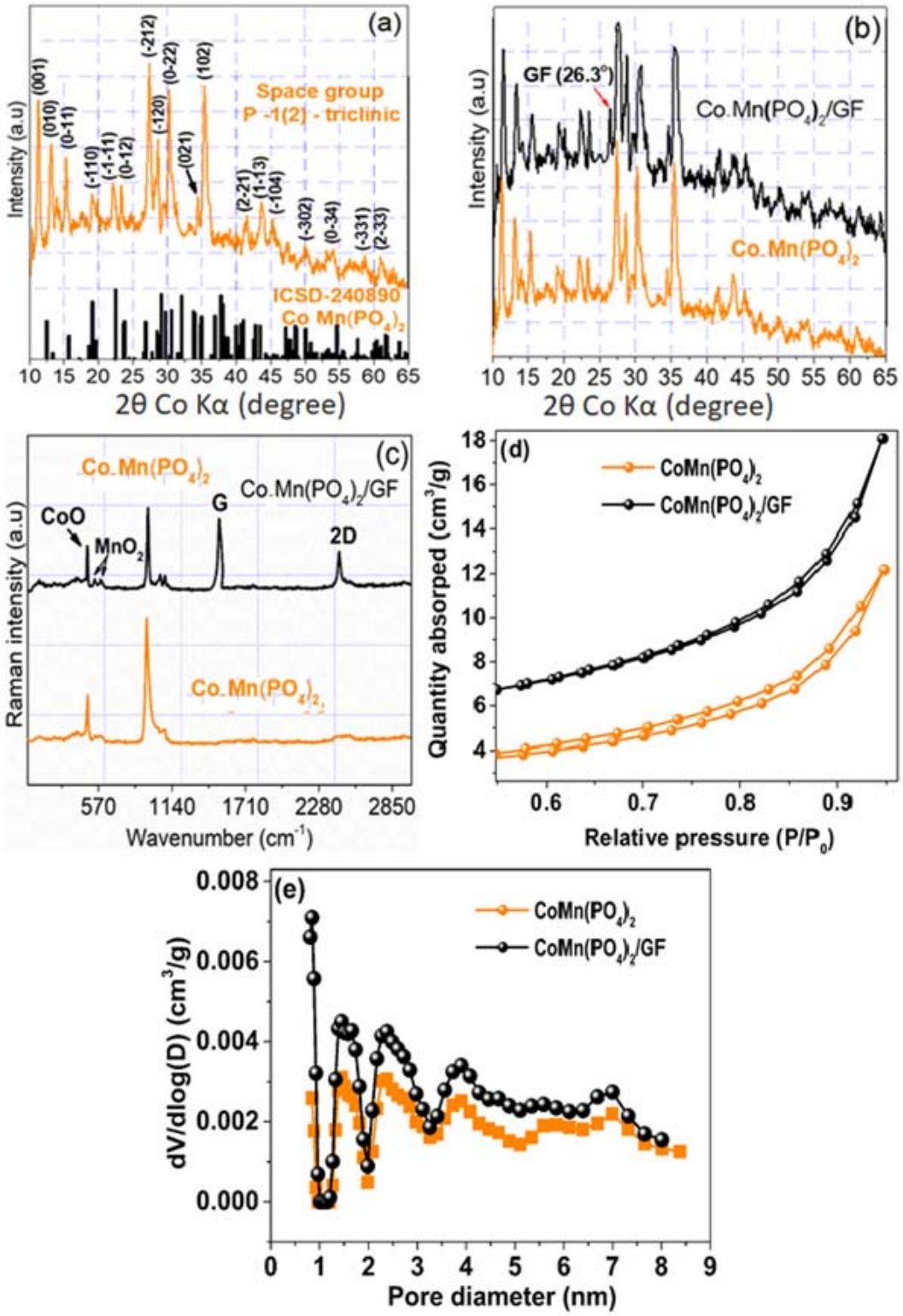

Fig. 1: X-ray diffraction patterns of (a) $CoMn(PO_4)_2$, (b) $CoMn(PO_4)_2$ plotted with CoMn(PO4)2/GF composite, (c) Raman spectra of $CoMn(PO_4)_2$ and $CoMn(PO_4)_2$/GF, (d) Isotherm and (e) Pore size distribution (PSD) analysis generated by Nitrogen adsorption/desorption of $CoMn(PO_4)_2$ and $CoMn(PO_4)_2$/GF.

The surface chemistry of $CoMn(PO_4)_2$/GF composite sample was examined by XPS as can be seen in Fig. 2. Fig. 2(a) shows XPS survey spectra of $CoMn(PO_4)_2$/GF composite sample which exhibit the main elements of the sample as (Mn 2p, Co 2p, P 2p, O 1s and C 1s). The sample shows atomic percentage of (7%) Mn 2p, (7.5%) Co 2p, (11.6%) P 2p, (15.7%) C 1s and (58.2%) O 1s indicating the sample is predominantly composed of oxygen however, the content of carbon on the surface is also reasonable. This suggest that the composite sample can be expected to possess a good electrical conductivity owing to the outstanding electrical conductivity of graphene.

Fig. 2(b), (c), (d), (e) and (f) show the high-resolution spectra of Mn 2p, Co 2p, P 2p, O 1s and C 1s respectively. The binding energy peaks detected at 642.11, 644.26, 653.11 and 655.05 eV in Fig. 2(b) comply with Mn $2p_{3/2}$, Mn $2p_{1/2}$ and satellite shakeup are associated to the chemical states of Mn^{2+} and Mn^{3+}. While the binding energy peaks detected at 782.72, 786.96, 799.12 and 804.08 eV in Fig. 2(c) comply with Co $2p_{3/2}$, Co $2p_{1/2}$ and satellite shakeup are associated to the chemical states of Co^{2+} and Co^{3+} [42]. The binding energy peaks positioned at 132.62 and 133.34 eV in Fig. 2(d) are assigned to P-P and P-O bonds respectively [43]. Fig. 2(e) shows the core level spectrum of O 1s with peaks detected at 530.81 and 531.96 eV which could be attributed to presence of Mn-O, Co-O and P-O compounds [44]. Fig. 2(f) displays C 1s core level spectrum of $CoMn(PO_4)_2$/GF composite sample. The binding energy peaks positioned at 283.92, 284.79, 285.41, 286.27 and 288.62 are associated to sp^2 C=C (graphene component), C−O−C, C=O, O−C=O (oxide components) and $\pi-\pi^*$ (satellite peak/electrons transition) bonding respectively. In this figure, all fitted peaks exhibit the sp^2 hybridization properties of graphene, traces of oxygen content present in GF and the $\pi-\pi^*$ electrons transition which enhances the C-C bonds in graphene and confirms the high quality of GF [45].

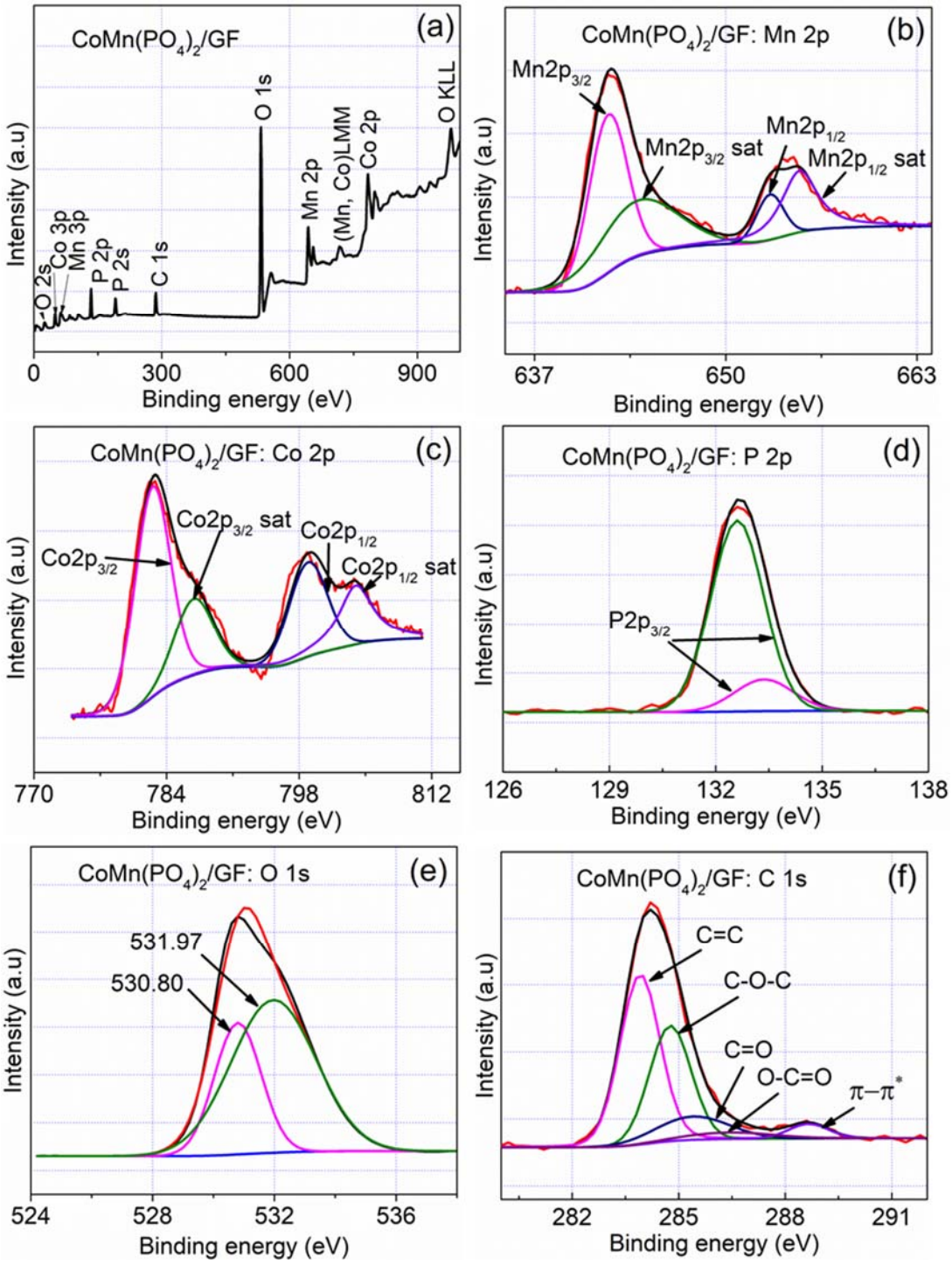

Fig. 2: (a) XPS survey spectra of $CoMn(PO_4)_2$/GF and high resolution spectra of (b) Mn 2p, (c) Co 2p, (d) P 2p, (e) O 1s and (f) C 1s of $CoMn(PO_4)_2$/GF.

SEM was used to obtain the morphology of $CoMn(PO_4)_2$ and $CoMn(PO_4)_2$/GF as presented in Fig. 3. Fig. 2(a & b) represents low and high magnifications SEM images of $CoMn(PO_4)_2$, where the sample shows a uniform flake-like morphology. Fig. 3(c) represents the TEM micrograph of $CoMn(PO_4)_2$, which is in-line with the flake-like images noticed in the SEM images shown in Fig. 3(a & b). The introduction of graphene foam (GF) into the matrix of the material did not change the morphology, however, a uniform and interconnected layered structure of the flake-like images were observed as displayed in Fig. 3 (d & e). This is clearly observed in the TEM micrograph of the sample as shown in Fig. 3 (c & f). The figure displays similar flake-like morphologies for both samples with attached sheets of graphene for the $CoMn(PO_4)_2$/GF sample (Fig. 3 (f)) . These layered structures of $CoMn(PO_4)_2$ were seen to form atop of the surface of GF sheets, thus covering the entire surface of the GF, which is why the GF could not be detected in the SEM images. In principle, SEM generates images caused by electron/atom interaction at the surface of the material, therefore might not be able to show the bottom GF sheets [26]. Fig. 3(f) signifies TEM micrograph of $CoMn(PO_4)_2$/GF at 50 nm, indicating the occurrence of graphene. The observed TEM micrograph in Fig. 3 (f) further confirmed the successful integration of graphene into $CoMn(PO_4)_2$ material.

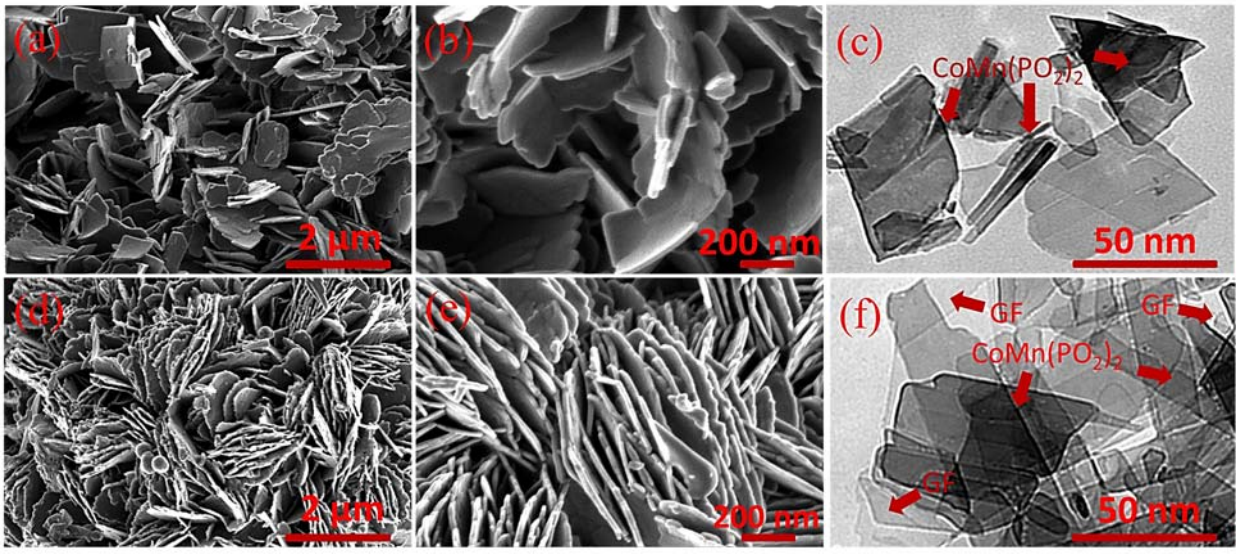

Fig. 3: (a & b) low (2 µm) and high (200 nm) magnification SEM images of $CoMn(PO_4)_2$, (c) TEM image of $CoMn(PO_4)_2$, (d & e) low (2 µm) and high (200 nm) magnification SEM images and (f) TEM image of $CoMn(PO_4)_2$/GF.

Fig. 4 (i) shows the EDX elemental composition of the $CoMn(PO_4)_2$/GF composite with the inset to the figure showing elemental wt%, while figure (ii) is the represents the elemental mapping of the $CoMn(PO_4)_2$/GF composite analyzed using energy dispersive X-ray mappings (EDX). Fig. 4 (ii (a)) shows the mutual elemental map of the composite while Fig. 4 (ii (b, c, d, e and f)) show the individual elemental map of Co, Mn, P, O and C, respectively. The observed maps proved a uniform dispersion of the elements within $CoMn(PO_4)_2$/GF composite sample.

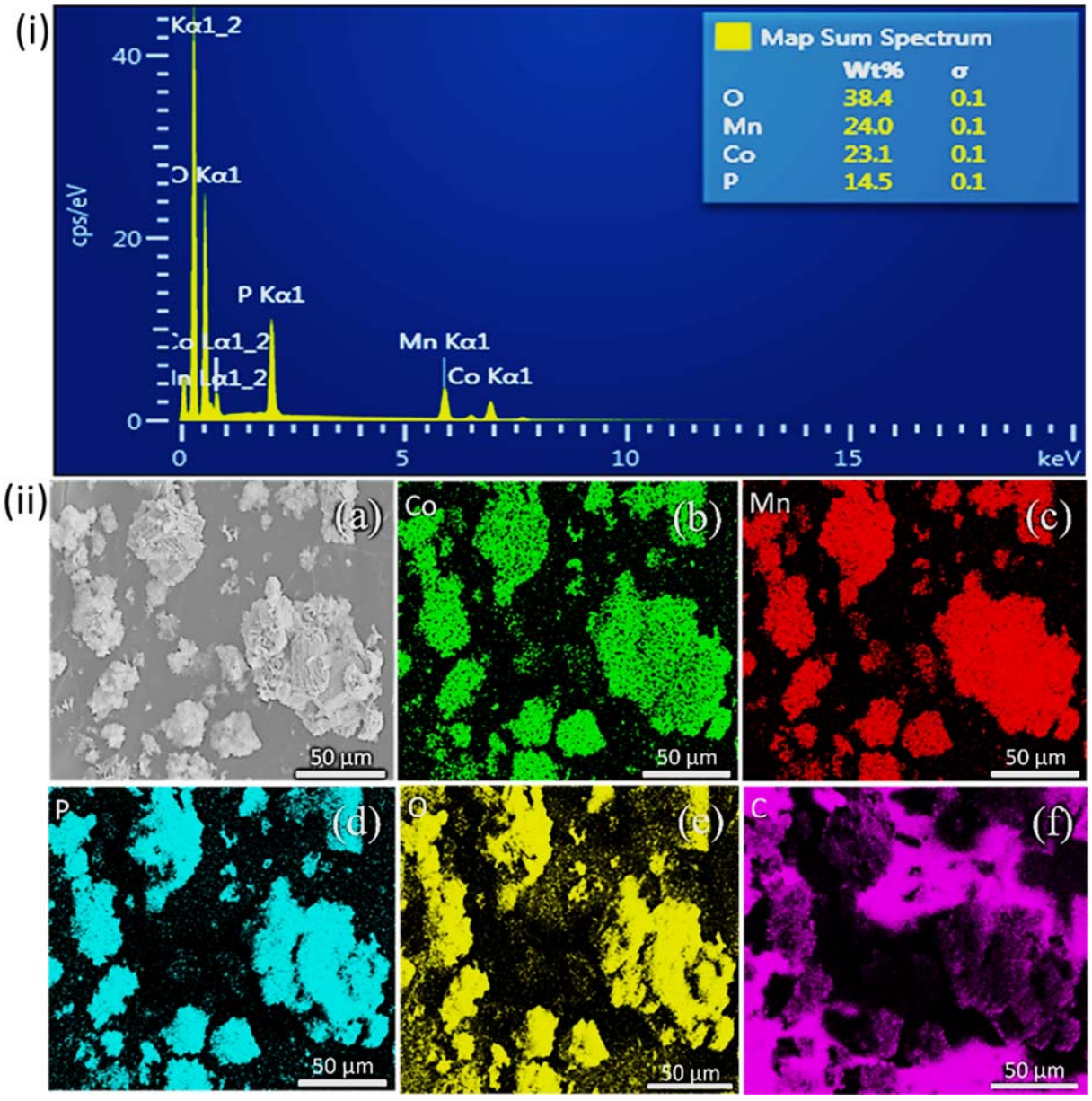

Fig. 4: (i) EDX spectrum of $CoMn(PO_4)_2$/GF composite and (ii) (a) EDX image of $CoMn(PO_4)_2$/GF composite, and EDX elemental mapping of (b) Co, (c) Mn, (d) P, (e) O and (f) C elements, respectively.

Fig. 5(a) displays a comparison of CV curves for $CoMn(PO_4)_2$ and $CoMn(PO_4)_2$/GF measured at the same 50 mV s^{-1}. The figure presents a larger curve area for $CoMn(PO_4)_2$/GF as against $CoMn(PO_4)_2$, indicating a higher current response for the composite sample compared to the pristine. The observed improved response for the composite is due to GF interaction in the composite sample. The integration of GF into $CoMn(PO_4)_2$ structure has resulted in a synergistic effect, enabling a defined sheet that seem to grow from GF base well separated and therefore enhances the flow of electrolyte ions in and out of the sheets. This in turn, reduces the possibility of sheets aggregation and minimizes ion diffusion resistance [27]. Fig. 5(b) presents GCD curves of both $CoMn(PO_4)_2$ and $CoMn(PO_4)_2$/GF where $CoMn(PO_4)_2$/GF is showing extended discharge time compared to $CoMn(PO_4)_2$ in line with CVs in Fig. 5(a). Fig. 5(c) presents EIS analysis for $CoMn(PO_4)_2$ and $CoMn(PO_4)_2$/GF. The Nyquist plots for $CoMn(PO_4)_2$ and $CoMn(PO_4)_2$/GF as shown in Fig. 5(c), reveal an estimated equivalent series resistance (ESR) (intercept to the x-axis in the high-frequency region) for both $CoMn(PO_4)_2$ and $CoMn(PO_4)_2$/GF of 0.95 Ω and 0.78 Ω, respectively. The lower ESR value of $CoMn(PO_4)_2$/GF compared to $CoMn(PO_4)_2$ is an evidence that the composite is less resistive as result of addition of the GF, which is also in line with the CVs and GCDs in Fig. 5(a and b). The charge transfer resistance (R_{CT}), results from ions interaction at the electrode-electrolyte interface. The non-noticeable semi-circle at high-frequency region indicates fast movements of ions and hence, a better capacitive performance. Moreover, in the low-frequency region, $CoMn(PO_4)_2$/GF shows the vertical line being closer to the imaginary axes (Z") as well as shorter diffusion length compared to $CoMn(PO_4)_2$, indicating a better capacitive characteristic of the composite.

Fig. 5(d) presents the CV profile of $CoMn(PO_4)_2$/GF at different scan rates of 5, 10, 20, 50 and 100 mV s^{-1} in a potential window range of 0.0 to 0.45 V. The CV shows the pseudocapacitive mechanism with no clear potential peaks [46], however, the charge is being stored through surface redox reaction (phase change process) between Co^{+} and Co^{3+} ($Co^{+} \leftrightarrow Co^{3+}$) and also Mn^{2+} and Mn^{3+} ($Mn^{2+} \leftrightarrow Mn^{3+}$) via the phase changing stated as equation (7 & 8):

$$CoMn(PO_4)_2 + OH^{-} \leftrightarrow CoMn(OH)(PO_4)_2 + e^{-} \quad \text{.....(7)}$$

$$CoMn(OH)(PO_4)_2 + OH^{-} \leftrightarrow CoMn(OH)_2(PO_4)_2 + e^{-} \quad \text{.....(8)}$$

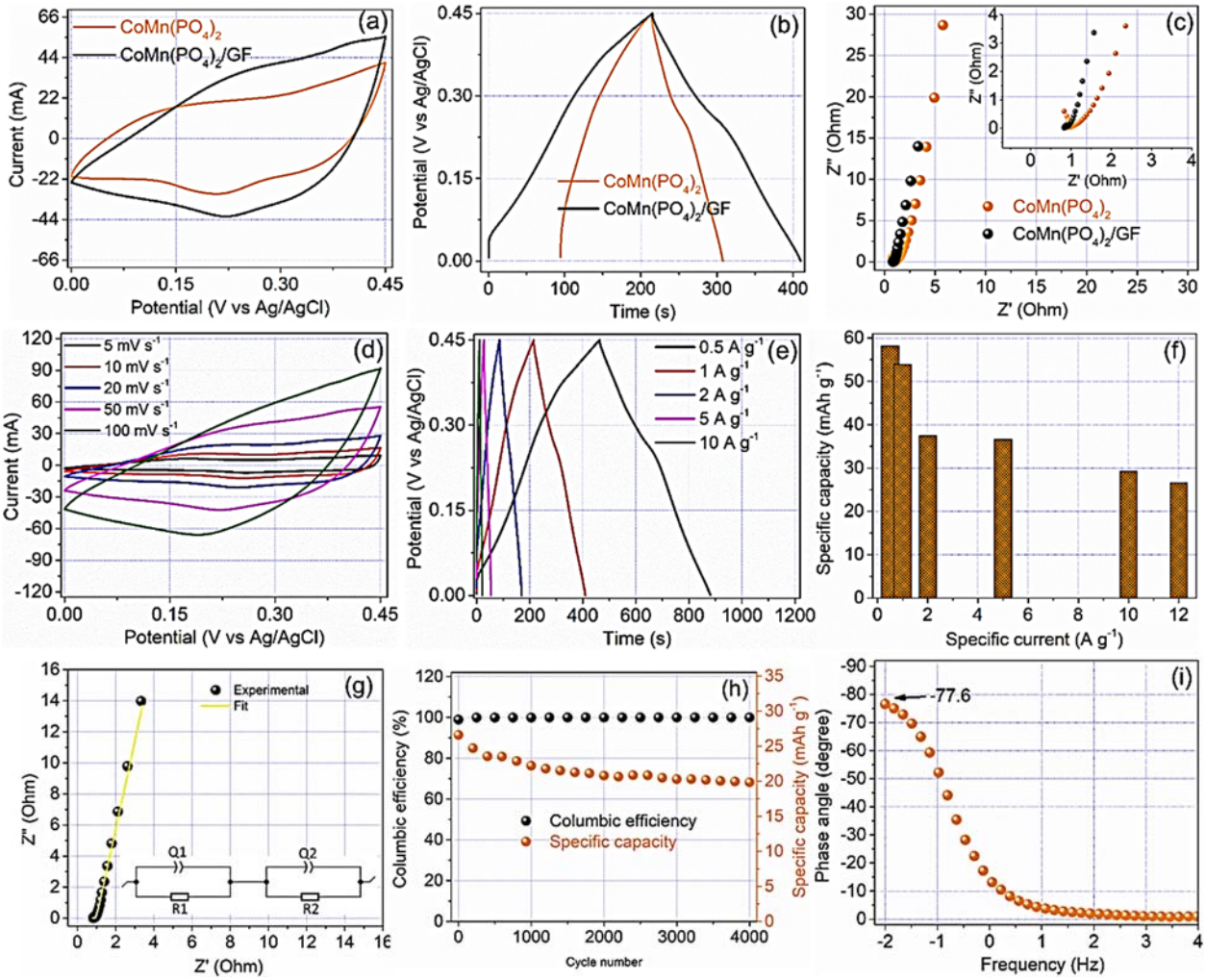

Fig. 5: (a and b) CV curves and GCD curves and (c) EIS of $CoMn(PO_4)_2$ and $CoMn(PO_4)_2$/GF respectively, (d and e) CV sweep at variety rates and GCD curves at variety specific-currents respectively, (f) specific capacity estimated in the range of specific currents for $CoMn(PO_4)_2$/GF sample, (g) fitted Nyquist plot with its corresponding circuit as the inset, (h) stability test in terms of specific capacity and Columbic efficiency and (i) phase angle as a function of frequency for $CoMn(PO_4)_2$/GF.

Afterwards, the capacitive performance of $CoMn(PO_4)_2$/GF was measured via the galvanostatic charge-discharge (GCD) technique and evaluated at 0.5, 1, 2, 5 and 10 A g^{-1} specific currents. As exposed in Fig. 5(e), the GCDs exhibit relatively symmetrical profile, which indicates a promising capacitive performance of $CoMn(PO_4)_2$/GF composite material. The associated CV and GCD shapes imply the pseudocapacitive nature of $CoMn(PO_4)_2$/GF composite material. Considering the GCDs in Fig. 5(e), the specific capacity values are calculated as shown in Fig. 5(f), where the

material achieved 58.15, 54.00, 37.46, 36.66, 29.22 and 26.82 mAh g^{-1} at of 0.5, 1, 2, 5, 10 and 12 A g^{-1} respectively.

The fitted Nyquist plot and its equivalent circuit (inset to Fig. 5(g)) are shown in Fig. 5(g). The fitting was carried out using a Z-fit program software attached to the Bio-Logic system used for electrochemical analysis. In the circuit, R1, which represents equivalent series resistant (ESR) is connected in parallel to Q1, which is the constant phase element (CPE) acting in the high-frequency region. R2, which represents charge transfer resistant (R_{CT}) is also in parallel to Q2, which represents mass-capacitance. The values of all the circuit elements are very close to the experimental data, therefore, give an excellent fit with the experimental data as depicted in Fig. 5(g).

The GCD cyclic stability test of $CoMn(PO_4)_2$/GF was performed for over 4000 cycles at 12 A g^{-1} (Fig. 5(h)). The double-Y plot in Fig. 5(h) shows that the material could retain about 75.3% of its initial specific capacity after a cycling test of 4000 cycles. Moreover, the material possesses outstanding columbic efficiency of nearly 100% with no noticeable fluctuations. The specific capacity was noticed to decline gradually until at about 2000 cycles when it then stabilized, this phenomenon could be referred to as wettability, which often takes place at the initial stages of the cycling [47]. Consequently, the material became more stable and this could be attributed to the interacting ions gaining full access to the pores of the material [28]. To evaluate the reliability of the material with the ideal capacitive nature, the phase angle was plotted as a function of frequency as could be seen in Fig. 5(i). The material showed a phase angle value of ~-77.3 degrees. This phase angle value indicates the material is of good properties as its closer to -90^o which considered being the ideal capacitive value.

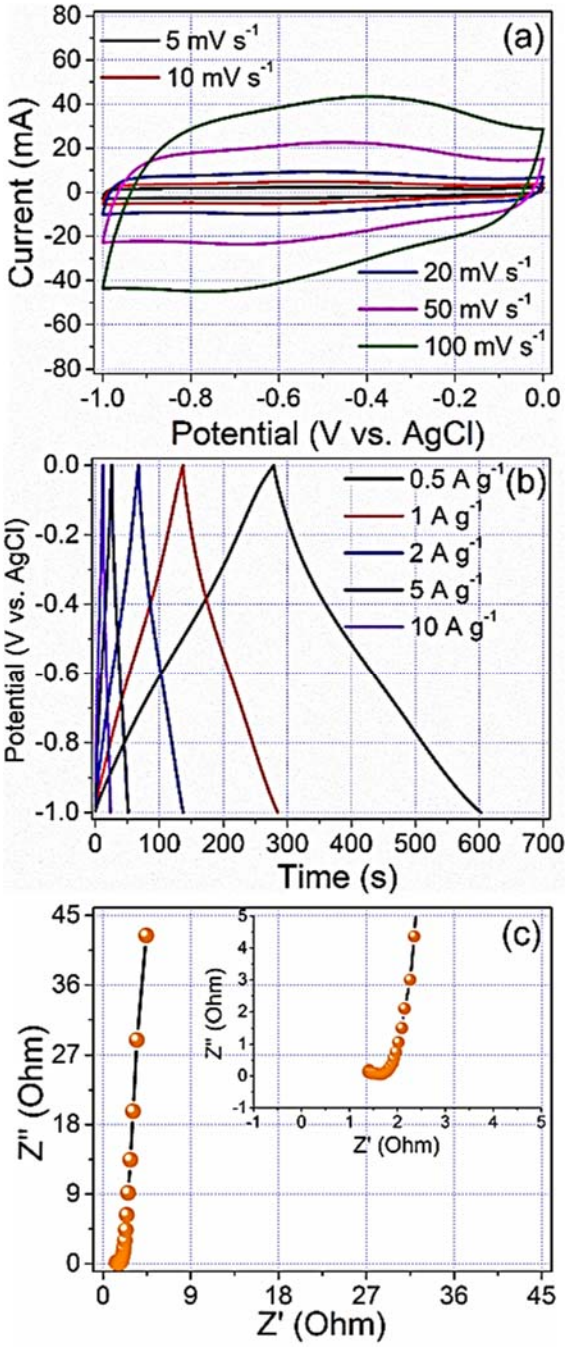

Fig. 6: (a) CV curves, (b) GCD curves and (c) EIS Nyquist plot of activated carbon (AC) derived from waste cocoa pods.

The CV, GCD and EIS of the AC applied as a negative electrode of the hybrid device were presented in Fig. 6. The observed CV curves measured within a potential range of -1.0 to 0.0 V displays a characteristic of EDLC nature. The current peak response of the material was witnessed to rise rapidly proportional to increase of scan rates from 5 mV s^{-1} to 100 mV s^{-1}, verifying the typical characteristics of carbon materials[29]. The observed behavior for the material (Fig. 6(a) was

further confirmed by the GCD in Fig. 6(b), where the material showing a symmetrically linear galvanostatic charge-discharge profile indicating the EDLC mechanism, which correlates to the CV curves in Fig. 6(a). The Nyquist plot of the AC is presented in Fig. 6(c). The Nyquist plot displays almost a vertical line, very close to Z”-axis with short diffusion path length, suggesting a promising electrode material for electrochemical capacitor. The equivalent series resistance (ESR) and charge transfer resistance (R_{CT}) of the material are estimated to be 1.3 Ω and 0.4 Ω, respectively, as can observed in the inset to the Fig. 6(c). The low ESR and R_{CT} values are indication that the AC material offers high electrical conductivity, which is essential for electrochemical capacitor. Based on the capacitive properties of the AC derived from waste cocoa pods, the material is expected to perform well in a hybrid device assembled with $CoMn(PO_4)_2$/GF as positive electrode. More details on the activated carbon derived from waste cocoa pods with their electrochemical performance are available in the literature [30,31,32].

Due to the $CoMn(PO_4)$/GF promising electrochemical results, the composite material was used as positive electrode in part with the activated carbon from waste cocoa pods (AC) as negative electrode to couple a hybrid device. Fig. 7 (a) represents CV profiles for both electrodes adopted in assembling of the device. The AC could work well in an operating potential range of -1.0 to 0.0 V, while the $CoMn(PO_4)$/GF works within the range of 0.0 to 0.45 V. Fig. 7(b) represents CV profile of $CoMn(PO_4)$/GF//AC hybrid device measured at a cell potential range of 0.0 to 1.5 V at scan rates ranging from 5 mV s^{-1} to 100 mV s^{-1} in 1 M KOH. The graph in Fig. 7(b) shows that $CoMn(PO_4)$/GF//AC hybrid device possesses two different features: EDLC signature at about 0.0–1.0 V and redox faradaic reaction at about 1.0–1.5 V, which reflect a contribution from the AC and $CoMn(PO_4)$/GF electrodes that made up the device. However, the EDLC characteristic has been overwhelmed by the faradic response at higher potential, therefore the device’s CV curves (Fig. 7(b)) portray a predominantly faradic behaviour. The noticed peaks at about 1.2 V and 1.4 V are due to the redox reaction of Co^{+} and Co^{3+} ($Co^{+} \leftrightarrow Co^{3+}$) and Mn^{2+} and Mn^{3+} ($Mn^{2+} \leftrightarrow Mn^{3+}$). Fig. 7(c) represents GCD profiles of the hybrid device at specific currents of 0.5 to 12 A g^{-1} measured within a cell potential of 0.0 to 1.5 V in line with CV profiles in Fig. 7(b). The GCD graphs in Fig. 7(c) reflect the faradic nature observed in Fig. 7(b) with a mixed performance of EDLC behavior at around 0.0 V to 1.0 V and faradic from about 1.0 V to 1.5V. The specific capacities at specific currents of 0.5, 1.0, 2.0, 5.0, 10 and 12 mV s^{-1} were calculated based on the area under

the discharge curve from the GCD in Fig. 7(c) using equation (1) and is shown in Fig. 7(d). The specific capacity values are 45.89, 44.31, 40.69, 26.15, 19.66 and 17.83 mAh g^{-1} at specific currents of 0.5, 1.0, 2.0, 5.0, 10 and 12 A g^{-1}, respectively.

The EIS Niquist plot of the device has been presented in Fig. 7(e). The plot shows an equivalent series resistance (ESR) value of 5.6 Ω, which is a mixture of electrode material's resistance, electrolyte's resistance, electrode/electrolyte interface resistance and electrode/current collector interface resistance [33,34]. Moreover, a charge transfer resistance value of 0.18 Ω was estimated due to phase transformation process results from the electron transfer. The inset to Fig. 7(e) is an equivalent circuit diagram used for fitting the experimental EIS data. In the circuit diagram, the equivalent series resistance (R_S) is in series with charge transfer resistance (R_{CT}), which is in parallel with real capacitance (Q_{CT}) [35]. At high-frequency region, a slight deviation from a real capacitance was noticed, which could be due to the leakage resistance (R_L), however the mass capacitance (Q_L) kept the line almost vertical close to the Z"-axes [36].

Fig. 7(f) represents a stability test in terms of columbic efficiency and specific capacity calculated at every 500 cycle for over 10000 GCD cycles at 12 A g^{-1}. The columbic efficiency showed approximately 100% after the long-term cycling test. In the initial stage, the specific capacity increased from 12.9 mAh g^{-1} to a maximum of 13.5 mAh g^{-1} and then started to decrease slightly until it reached 12.3 mAh g^{-1} at the 10000th cycle giving an efficiency of ~ 95%. The initial increase might be explained as the ions are not fully capable of accessing the material's pore at the initial cycles, the pores are being accessible with time, leading to an intimate contact at the electrode/electrolyte edge. The voltage holding test is an established alternative and dependable technique for analyzing the stability of supercapacitor electrodes. It provides a factually correct resistance effect after being subjected to maximum potential, which may be near to practical application [48]. The test proffers a direct insight into the probable effect and degradation phenomena that might occur during the electrochemical process in cells at significant potentials in comparison with the conventional cycling test that often provides no degradation [48]. Here in, the method was carried out at a constant load by holding the device at its highest operating potential (1.5 V) and estimating the capacitance over the entire period as shown in Fig. 7 (g) in a repeated sequence. Fig. 7(g) presents a plot of the voltage holding test of $CoMn(PO_4)$/GF//AC

hybrid device investigated at 2 A g^{-1} in an operating potential of 1.5 V for 110 h. The capacity of the device calculated after every 10 h and throughout 110 h was recorded and showed in the figure. The figure showed that the specific capacity was increasing until 20 h then stabilized at about 40 mAh g^{-1} with a slight increase for the rest of the floating time. The hybrid device reached a specific capacity of ~41.0 mAh g^{-1} after a voltage holding test for over 110 h at a specific current of 2 A g^{-1}. An increase of 2.5 % compared to a specific capacity of ~40.0 mAh g^{-1} obtained for the device before the voltage holding test. The excellent long term stability observed in the form of capacity retention (Fig. 7(f)) and voltage holding (Fig. 7(g)) can be explained based on the following two aspects: (1) The structure of $CoMn(PO_4)$ is chemically stable due to the P-O strong covalent bond that cannot be destroyed easily and (2) the high stability of AC which strongly synergizes with $CoMn(PO_4)$ when coupled in $CoMn(PO_4)$/GF//AC hybrid device.

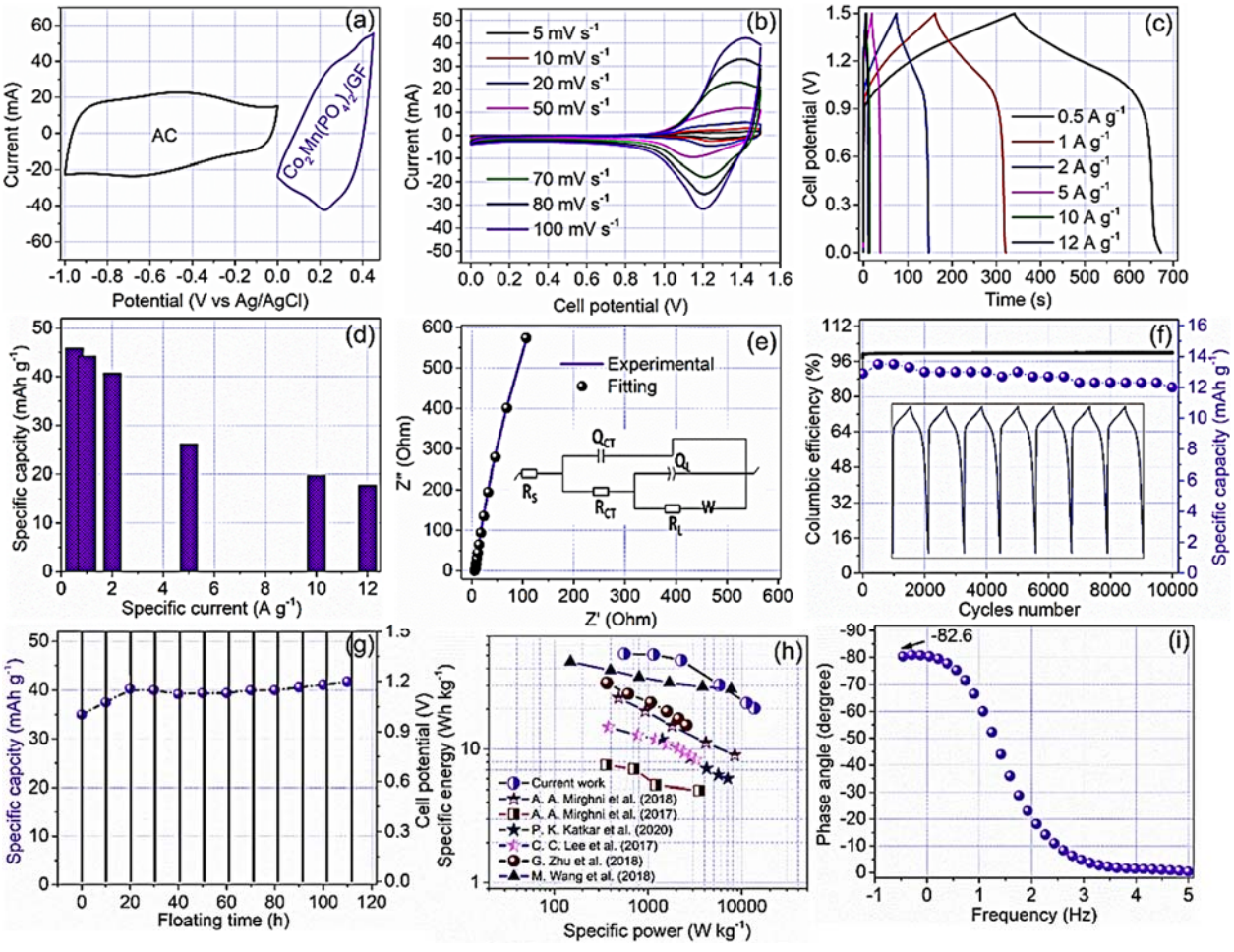

Fig. 7: (a) CV profile of AC and $CoMn(PO_4)$/GF, (b, c) CV and GCD, (d) Specific capacity values at different specific currents, (e) EIS and (inset to the figure) showing the corresponding circuit applied to fit the data, (f) cycling test

presented in terms of retention and efficiency, (g) stability test presented as voltage holding, (h) Ragone plot compares the current work with other similar works from the literature and (i) phase angle as function of frequency of $CoMn(PO_4)_2$/GF//AC device.

Fig. 7(h) expresses a Ragone plot matching the current hybrid device's performance with other metal phosphates device's performance described in the literature work. The $CoMn(PO_4)_2$/GF//AC hybrid device shows a maximum specific energy values of 51.5 Wh kg^{-1} equivalent to a specific power of 561.5 W kg^{-1} at 0.5,. These values are much higher compared to other metal phosphate-based devices as shown in Fig. 7(h), and in Table 1 [10,16,37-40]. Therefore, $CoMn(PO_4)_2$ can strongly be considered as promising pseudocapacitive material other than well-known materials such as MnO_2 and RuO_2 for electrochemical capacitors. Fig. 7(i) represents a plot of the phase angle versus frequency of $CoMn(PO_4)_2$/GF//AC hybrid device, showing a phase angle -82.6°. The obtained value is close to the ideal capacitive value of -90°, which further evident that the device's electrochemical performance is of great potential for electrochemical capacitors.

Table 1: $CoMn(PO_4)_2$/GF//AC hybrid device's performance and other metal phosphate-based devices from the literature.

Device	**Max. specific energy (Wh kg^{-1})**	**Max. specific Power (W kg^{-1})**	**Cycle number**	**Capacitance/Capacity retention (%)**	**Ref.**
$Mn_3(PO_4)_2$// $Mn_3(PO_4)_2$	11.7	1410	9000	99	[10]
AC//PANI- $Mn_3(PO_4)_2$	14.7	378	3000	80	[37]
$Co_3(PO_4)_2.4H_2O$/GF//CFP	24	468	10000	99	[38]
AC//$Mn_3(PO_4)_2$/100 mg GF	7.6	360	10000	96	[16]
NCoNIP@NCoNIP//HPC	44.6	150	7000	77.5	[39]
Mn-CoP//AC	35.21	193	4000	88.9	[40]
$CoMn(PO_4)_2$/GF//AC	51.5	561.5	10000	95	Current work

4 Conclusion

$CoMn(PO_4)_2$ and $CoMn(PO_4)_2$/GF composites were effectively synthesized via a hydrothermal method. The crystal structure, vibrational and rotational modes and composition and chemical bond configuration of the sample were acquired and discussed by means of XRD, Raman spectroscopy and XPS. The morphology and microstructure of the samples were carried out using SEM and TEM while the elemental mapping was carried out using EDX maps attached to SEM. The study demonstrates the electrochemical properties of a combination of well-established pseudocapacitive materials (Co-phosphate, Mn-phosphate). Even though, the discrete electrochemical storage mechanism of Mn and Co is redox reaction however, each of the metals possesses semi-rectangular CV sweep and semi-linear GCD due to the polarization initiated from polar nature of the materials. Moreover, graphene was introduced to the matrix of the material to further develop the conductivity and surface texture. The $CoMn(PO_4)_2$/GF composite material was tested with 1 M KOH electrolyte in both half and full cell configuration. For the half-cell, the $CoMn(PO_4)_2$/GF achieved a maximum a specific capacity of 58.15 mAh g^{-1} at 0.5 A g^{-1}. Therefore, $CoMn(PO_4)_2$/GF was used as positive electrode and AC as negative electrode in a hybrid device. The $CoMn(PO_4)_2$/GF//AC hybrid device achieved a maximum a specific capacity of 45.89 mAh g^{-1}, a specific energy of 51.53 Wh kg^{-1} and a specific power of 561.52 W kg^{-1} at 0.5 A g^{-1}. The device after been subjected to stability test in the form of GCD cycling could retain 95% of its initial specific capacity for over 10000 cycles at 12 A g^{-1} and also showed increase over its initial specific capacity after a voltage holding test for over 110 h at 2 A g^{-1}. The electrochemical results achieved in this study indicated that $CoMn(PO_4)_2$ material is of great prospective as pseudocapacitive material for supercapacitor applications.

Acknowledgements

This work is based on research supported by the South African Research Chairs Initiative (SARChI) of the Department of Science and Technology and the National Research Foundation (NRF) of South Africa (Grant No. 61056). Any opinion, finding and conclusion or recommendation expressed in this work is that of the author(s) and the NRF does not accept any liability in this

regard. Abdulmajid A. Mirghni acknowledges the financial support from the University of Pretoria, the NRF through the SARChI in Carbon Technology and Materials, and Al Fashir University, Sudan.

Data availability

The data that support the findings of this study are available from the corresponding author upon reasonable request.

References

[1] Conway B.E., Electrochemical Supercapacitors_Scientific Fundamentals and Technological Applications, Springer, Boston, USA 1999.

[2] Hathaway D.H., Eddy J.A., Petrovay K., Vaquero J.M., Gallego M.C., Usoskin I.G., Solanki S.K., Usoskin I.G., Kromer B., Usoskin I.G., S.K. Solanki, Kovaltsov G.A., Steinhilber F., Abreu J.A., Beer J., Abreu J.A., Beer J., Steinhilber F., Tobias S.M., Lockwood M., Hoyt D. V, Schatten K.H., True Performance Metrics in Electrochemical Energy Storage, Science (80-.). **334** (2011) 917–918.

[3] Miller J.R., Simon P., Materials science: Electrochemical capacitors for energy management, Science (80-.).

[4] Li X., Elshahawy A.M., Guan C., Wang J., Metal Phosphides and Phosphates-based Electrodes for Electrochemical Supercapacitors, Small, **13** (2017) 1–24.

[5] Structures O., Natarajan S., Mandal S., Open-Framework Structures of Transition-Metal Compounds Angewandte, Angew. Chem. Int. Ed., **47** (2008) 4798–4828.

[6] Cohpo F., Few-layered CoHPO 4 $ 3H 2 O ultrathin nanosheets for high performance of electrode materials for supercapacitors, Nanoscale, **5** (2013) 5752–5757.

[7] Feng L., Xue H., Advances in Transition-Metal Phosphide Applications in Electrochemical Energy Storage and Catalysis, ChemElectroChem. **4** (2017) 20–34.

[8] Chang Y., Shi N.E., Zhao S., Xu D., Liu C., Tang Y.J., Dai Z., Lan Y.Q., Han M., Bao J., Coralloid CoP_2O_7 Nanocrystals Encapsulated by Thin Carbon Shells for Enhanced Electrochemical Water Oxidation, ACS Appl. Mater. Interfaces. **8** (2016) 22534–22544.

[9] Qin X., Yan B., Yu J., Jin J., Tao Y., Mu C., Wang S., Xue H., Pang H., Phosphorus-based materials for high-performance rechargeable batteries, Inorg. Chem. Front. **4** (2017) 1424–1444.

[10] Katkar P.K., Marje S.J., Pujari S.S., Khalate S.A., Deshmukh P.R., Patil U.M., Single-pot hydrothermal synthesis of manganese phosphate microrods as a cathode material for highly stable flexible solid-state symmetric supercapacitors, Synth. Met. **267** (2020) 116446.

[11] Gou J., Du Y., Xie S., Liu Y., Kong X., Easily-prepared bimetallic metal phosphides as high-performance electrode materials for asymmetric supercapacitor and hydrogen evolution reaction, Int. J. Hydrogen Energy. **44** (2019) 27214–27223.

[12] Zhang N., Li Y., Xu J., Li J., Wei B., Ding Y., Amorim I., Thomas R., Thalluri S.M., Liu Y., Yu G., Liu L., High-Performance Flexible Solid-State Asymmetric Supercapacitors Based on Bimetallic Transition Metal Phosphide Nanocrystals, ACS Nano. **13** (2019) 10612–10621.

[13] Mirghni A.A., Oyedotun K.O., Olaniyan O., Mahmoud B.A., Manyala N., Electrochemical analysis of Na – Ni bimetallic phosphate electrodes for supercapacitor applications, RSC Adv. **9** (2019) 25012–25021.

[14] Mirghini A. A., Oyedotun K.O., Ahmed B., Bello A., Ray S.C., Manyala N., Nickel-cobalt phosphate/graphene foam as enhanced electrode for hybrid supercapacitor, Compos. Part B. **174** (2019) 106953.

[15] Chinnadurai D., Selvaraj A.R., Rajendiran R., Kumar G.R., Kim H.J., Viswanathan K.K., Prabakar K., Inhibition of Redox Behaviors in Hierarchically Structured Manganese Cobalt Phosphate Supercapacitor Performance by Surface Trivalent Cations, ACS Omega. **3** (2018) 1718–1725.

[16] Mirghni A.A., Madito M.J., Masikhwa T.M., Oyedotun K.O., Bello A., Manyala N., Hydrothermal synthesis of manganese phosphate/graphene foam composite for electrochemical supercapacitor applications, J. Colloid Interface Sci. (2017), **494,** 325.

[17] Noori A., El-Kady M.F., Rahmanifar M.S., Kaner R.B., Mousavi M.F., Towards establishing

standard performance metrics for batteries, supercapacitors and beyond, Chem. Soc. Rev. **48** (2019) 1272–1341.

[18] EC-lab Software User's Manual 2014, Version 11.34.

[19] Bates S., Zografi G., Engers D., Morris K., Crowley K., Newman A., Analysis of amorphous and nanocrystalline solids from their X-ray diffraction patterns, Pharm. Res. **23** (2006) 2333–2349.

[20] Shende T.P., Bhanvase B.A., Rathod A.P., Pinjari D. V., Sonawane S.H., Sonochemical synthesis of Graphene-Ce-TiO2 and Graphene-Fe-TiO2 ternary hybrid photocatalyst nanocomposite and its application in degradation of crystal violet dye, Ultrason. Sonochem. **41** (2018) 582–589.

[21] Baril M., Assaaoudi H., Butler I.S., Pressure-tuning Raman microspectroscopic study of cobalt(II), manganese(II), zinc(II) and magnesium(II) pyrophosphate dihydrates, J. Mol. Struct. **751** (2005) 168–171.

[22] Ramana C. V., Ait-Salah A., Utsunomiya S., Backer U., Mauger A., Gendron F., Julien C.M., Structural characteristics of lithium nickel phosphate studied using analytical electron microscopy and raman spectroscopy, Chem. Mater. **18** (2006) 3788–3794.

[23] Chapman C., Thirlwell L.E., The infra-red spectra ot orthophosphates, Spectrochim. Acta. **20** (1964) 937–947.

[24] Vlassiouk I., Smirnov S., Ivanov I., Fulvio P.F., Dai S., Meyer H., Chi M., Hensley D., Datskos P., Lavrik N. V., Electrical and thermal conductivity of low temperature CVD graphene : the effect of disorder, **27** (2011) 1.

[25] Sing K.S.W., Williams R.T., Physisorption hysteresis loops and the characterization of nanoporous materials, Adsorpt. Sci. Technol. **22** (2004) 773–782.

[26] Kleebe H.J., Comparison between SEM and TEM imaging techniques to determine grain-boundary wetting in ceramic polycrystals, J. Am. Ceram. Soc. **85** (2002) 43–48.

[27] Chen C., Liang T., Chen X., Zhang B., Wang L., Zhang J., Phosphorus-assisted solid-phase approach to three-dimensional highly porous graphene sheets and their capacitance properties, Carbon N. Y. **132** (2018) 8–15.

[28] Hong J., Lee Y.W., Ahn D., Pak S., Lee J., Jang A.R., Lee S., Hou B., Cho Y., Morris S.M., Shin H.S., Cha S.N., Sohn J.I., Kim J.M., Highly stable 3D porous heterostructures with hierarchically-coordinated octahedral transition metals for enhanced performance supercapacitors, Nano Energy. **39** (2017) 337–345.

[29] Frackowiak E., Carbon materials for supercapacitor application, Phys. Chem. Chem. Phys. **9** (2007) 1774–1785.

[30] Yetri Y., Hoang A.T., Mursida, Dahlan D., Muldarisnur, Taer E., Chau M.Q., Synthesis of activated carbon monolith derived from cocoa pods for supercapacitor electrodes application, Energy Sources, Part A Recover. Util. Environ. Eff., **00** (2020) 1–15.

[31] Daud Z., Sari A., Kassim M., Aripin A.M., Awang H., Hatta Z.M., Education V., Tun U., Onn H., Pahat B., Chemical Composition and Morphological of Cocoa Pod Husks and Cassava Peels for Pulp and Paper Production, Aust. J. Basic Appl. Sci. **7** (2013) 406–411.

[32] Pangarso Z.D., Cahyaningsih L., Imam K., Kurnia F., Purwaningsih D., Nano Carbon-based as Supercapacitor Electrode from Cocoa Skin, **3** (2020) 175–178.

[33] Mei B.A., Munteshari O., Lau J., Dunn B., Pilon L., Physical Interpretations of Nyquist Plots for EDLC Electrodes and Devices, J. Phys. Chem. C. **122** (2018) 194–206.

[34] Noori A., El-Kady M.F., Rahmanifar M.S., Kaner R.B., Mousavi M.F., Towards establishing standard performance metrics for batteries, supercapacitors and beyond, Chem. Soc. Rev. **48** (2019) 1272–1341.

[35] Sun W., Chen X., Preparation and characterization of polypyrrole films for three-dimensional micro supercapacitor, **193** (2009) 924–929.

[36] Li H., Wang J., Chu Q., Wang Z., Zhang F., Wang S., Theoretical and experimental specific capacitance of polyaniline in sulfuric acid, **190** (2009) 578–586.

[37] Lee C.C., Omar F.S., Numan A., Duraisamy N., Ramesh K., Ramesh S., An enhanced performance of hybrid supercapacitor based on polyaniline-manganese phosphate binary composite, J. Solid State Electrochem. **21** (2017) 3205–3213.

[38] Mirghni A.A., Momodu D., Oyedotun K.O., Dangbegnon J.K., Manyala N., Electrochemical analysis of Co3(PO4)2·4H2O/graphene foam composite for enhanced capacity and long cycle life hybrid asymmetric capacitors, Electrochim. Acta. **283** (2018) 374-384.

[39] Wang M., Zhao Y., Zhang X., Qi R., Shi S., Li Z., Wang Q., Zhao Y., Interface-rich core-shell ammonium nickel cobalt phosphate for high-performance aqueous hybrid energy storage device without a depressed power density, Electrochim. Acta. **272** (2018) 184–191.

[40] Zhu G., Yang L., Wang W., Ma M., Zhang J., Wen H., Zheng D., Yao Y., Hierarchical three-dimensional manganese doped cobalt phosphide nanowire decorated nanosheet cluster arrays for high-performance electrochemical pseudocapacitor electrodes, Chem. Commun. **54** (2018) 9234–9237.

[41] Simon P., Gogotsi Y., Materials for electrochemical capacitors, **7** (2008) 1–10. doi:10.1038/nmat2297.

[42] Gao Y, Mi L, Wei W, Cui S, Zheng Z, Hou H, et al. Double metal ions synergistic effect in hierarchical multiple sulfide microflowers for enhanced supercapacitor performance. ACS Appl Mater Interfaces **7** (2015) 4311–9.

[43] You A, Be MAY. In I. Studies of the oxidation states of phosphorus gettered silicon substrates using X- ray photoelectron spectroscopy and transmission electron microscopy. J Appl Phys **113** (2013) 1–7.

[44] Qiu C, Ai L, Jiang J. Layered phosphate-incorporated nickel cobalt hydrosilicates for highly Efficient oxygen evolution electrocatalysis. ACS Sustainable Chem Eng **6** (2018) 4492–8.

[45] Mirghni AA, Madito MJ, Oyedotun KO, Masikhwa TM, Ndiaye NM, Ray SJ, et al. A high energy density asymmetric supercapacitor utilizing a nickel phosphate/ graphene foam composite as the cathode and carbonized iron cations adsorbed onto polyaniline as the anode. RSC Adv **8** (2018) 11608–21.

[46] Shao Y., El-Kady M. F., Sun J., Li Y., Zhang Q., Zhu M., Wang H., Dunn B., and Kaner R. B., Design and mechanisms of asymmetric supercapacitors, Chem. Rev. **118** (2018) 9233-9280.

[47] Bello A., Fashedemi O. O., Lekitima J. N., Fabiane M., Dodoo-Arhin D., Ozoemena K. I., Gogotsi Y., Johnson A. T. C., and Manyala N., High-performance symmetric electrochemical capacitor based on graphene foam and nanostructured manganese oxide, AIP Advances **3** (2013) 082118-9.

[48] Kabir O. Oyedotun, Tshifhiwa M. Masikhwa, Abdulmajid A. Mirghni, Bridget K. Mutuma, Ncholu Manyala, Electrochemical properties of asymmetric supercapacitor based onoptimized carbon-based nickel-cobalt-manganese ternary hydroxide and sulphur-doped carbonized iron-polyaniline electrodes, Electrochimica Acta **334** (2020) 135610.